The Astronomical Journal, 149:113 (11pp), 2015 March doi:10.1088/0004-6256/149/3/113

SIZE AND SHAPE FROM STELLAR OCCULTATION OBSERVATIONS OF THE DOUBLE JUPITER TROJAN PATROCLUS AND MENOETIUS

Marc W. Buie[1], Catherine B. Olkin[1], William J. Merline[1], Kevin J. Walsh[1], Harold F. Levison[1], Brad Timerson[2], Dave Herald[3], William M. Owen Jr.[4], Harry B. Abramson[2], Katherine J. Abramson[2], Derek C. Breit[5], D. B. Caton[6], Steve J. Conard[2], Mark A. Croom[7], R. W. Dunford[2], J. A. Dunford[2], David W. Dunham[8], Chad K. Ellington[9], Yanzhe Liu[10], Paul D. Maley[11], Aart M. Olsen[2], Steve Preston[2], Ronald Royer[2], Andrew E. Scheck[2], Clay Sherrod[12], Lowell Sherrod[12], Theodore J. Swift[2], Lawrence W. Taylor III[7], and Roger Venable[2]

[1] Southwest Research Institute, 1050 Walnut St., Suite 300, Boulder, CO 80302, USA; buie@boulder.swri.edu
[2] International Occultation Timing Association (IOTA); btimerson@rochester.rr.com, Harry.Kat86@cox.net, steve.conard@comcast.net, aartmolsen@comcast.net, stevepr@acm.org, ronroy@springvillewireless.com, schecae1@gmail.com, tjswift@omsoft.com, rjvmd@hughes.net, bargonne@gmail.com
[3] 3 Lupin Pl., Murrumbateman, NSW, Australia; DRHerald@bigpond.net.au
[4] JPL, CA, USA; wmo@jpl.nasa.gov
[5] IOTA/Breit Ideas Observatory, Morgan Hill, CA, USA; breit_ideas@poyntsource.com
[6] Dark Sky Observatory, Dept. of Physics and Astronomy, Appalachian State University, Boone, NC 28608, USA; catondb@appstate.edu
[7] NASA Langley Research Center, Hampton, VA 23681, USA; mark.a.croom@nasa.gov, lawrence.w.taylor@nasa.gov
[8] IOTA, 7913 Kara Ct., Greenbelt, MD 20770, USA; dunham@starpower.net
[9] IOTA/Fundamental Chief Observatory, 1267 Sheridan Dr., Owings, MD 20736, USA; ckellington@gmail.com
[10] 1190 S. Bernardo Ave., Sunnyvale, CA 94087, USA; liuyanzhe@gmail.com
[11] IOTA, Houston, TX, USA; pdmaley@yahoo.com
[12] IOTA, Arkansas Sky Observatories; drclay@tcworks.net
Received 2014 November 9; accepted 2015 January 21; published 2015 February 26

ABSTRACT

We present results of a stellar occultation by the Jupiter Trojan asteroid Patroclus and its nearly equal size moon, Menoetius. The geocentric mid-time of the event was 2013 October 21 06:43:02 UT. Eleven sites out of 36 successfully recorded an occultation. Seven chords across Patroclus yielded an elliptical limb fit of 124.6 by 98.2 km. There were six chords across Menoetius that yielded an elliptical limb fit of 117.2 by 93.0 km. There were three sites that got chords on both objects. At the time of the occultation we measured a separation of 664.6 km (0.247 arcsec) and a position angle for Menoetius of 265°.7 measured eastward from J2000 north. Combining this occultation data with previous light curve data, the axial ratios of both objects are 1.3 : 1.21 : 1, indicative of a mostly oblate ellipsoid with a slight asymmetry in its equatorial projection. The oblate shape is not an equilibrium shape for the current rotation period, but would be if it were rotating with an ~8 h period. This faster period is consistent with a pre-evolved state of the system with an orbital separation that is 50% smaller. Our best estimate of the system density is 0.88 g cm^{-3}.

Key words: astrometry – minor planets, asteroids: individual (Patroclus, Menoetius) – occultations

1. INTRODUCTION

Discovered in 1906, (617) Patroclus was the second Jupiter Trojan found and is among the largest of this dynamical class of objects. See Mueller et al. (2010) for a good review of this object. The observational history of Patroclus is rather sparse, especially considering that it is a reasonably bright and easily observed target that has been known for over 100 yr. Interest in Patroclus was significantly increased when a satellite was discovered by direct imaging (Merline et al. 2001a) in 2001 with followup in 2002. These observations showed two objects of similar brightness (delta mag ~0.2). There is one object that is consistently brighter, and the brighter of the two has always been considered to be the primary object, Patroclus. A report on the discovery and initial orbit solution was given orally at that time (Merline et al. 2001b). The initial orbital parameters, density, and size estimates of 95 and 105 km were given by Merline et al. (2002). Additional observations were obtained in 2004–2005 that further refined the orbit (Marchis et al. 2006). Adaptive optics (AO) observations of the system were also obtained just prior to the occultation in 2013 by a team led by Merline.

Oey (2012) observed Patroclus in 2011 August and derived a light curve period of 103.5 ± 0.3 h with an amplitude of 0.06 ± 0.02 mag. This compares well with Mueller et al. (2010), who reported observations taken in 1996 April and derived a period of 103.02 ± 0.40 h with an amplitude of 0.070 ± 0.005 mag. The period is based on a double-peaked, shape-dominated interpretation of the light curve that was explained by an ellipsoidal shape with axial ratios of 1.07 : 1.0 : 1.0. There are no other periodicities noted leading to the conclusion that the two components of the system are in synchronous rotation locked to the orbit period. The orbit, and thus, rotation poles, were well enough determined to successfully predict mutual events that enabled thermal infrared observations with the *Spitzer Space Telescope* (*SST*) in 2006 June. These data led to derivation of thermo-physical properties of the surfaces of both objects (Mueller et al. 2010). The observations are consistent with identical surface regolith properties. The *SST* observations did not resolve the system though they did observe shadowing on each object in two different events. The thermal observations indicate a combined surface-area-equivalent diameter of 145 ± 15 km (Mueller et al. 2010). Apparently, optical observations of the mutual events were also observed at the same epoch (Berthier et al. 2007). These observations and results are as-yet unpublished though the work is cited heavily in Mueller et al. (2010).

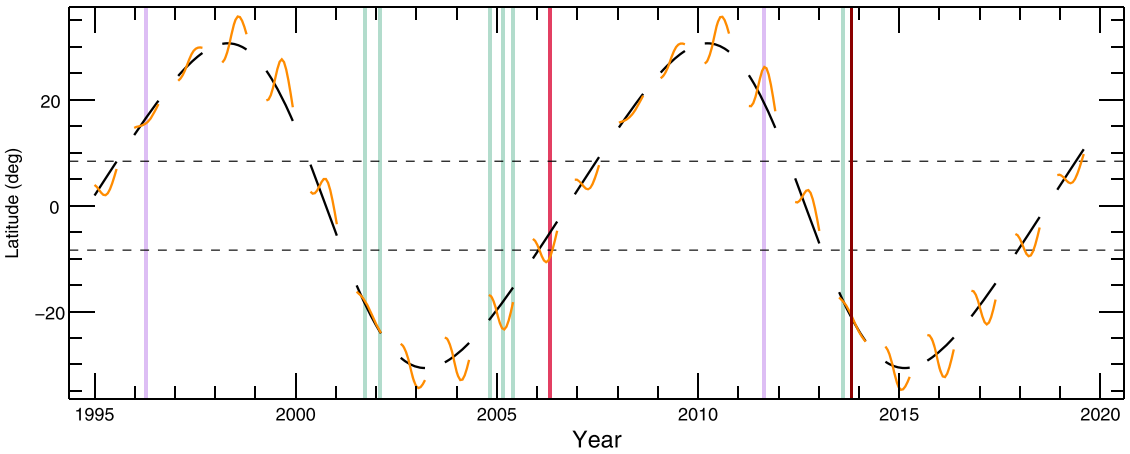

Figure 1. Sub-Earth and Sub-solar latitude on Patroclus vs. time. The sub-solar latitude is plotted as a black line. The sub-Earth latitude is plotted as an orange line. The curves are drawn only when the object is observable—when the solar elongation is greater than 60°. The vertical lines indicate the time of different data sets: purple is for light curve data, green is for resolved imaging of the system, red is for thermal infrared observations during a mutual event. The right-most dark red line is the time of the occultation.

For our analysis we will assume a fully tidally evolved system with rotation poles coincident with the orbit pole. Thus, the latitude of the viewpoint is also the opening angle of the projected ellipse of the orbit. Figure 1 shows the sub-Earth and sub-solar latitude as a function of time that spans most of the relevant observations of this system. The geometry is based on an orbit solution, provided by Owen and presented by Merline et al. (2001b), with an orbit pole of $\alpha = 335\overset{\circ}{.}6$, $\delta = 71\overset{\circ}{.}9$ in an Equatorial J2000 reference frame. The latitudes are plotted only when the solar elongation of Patroclus is greater than 60°. The smoothly varying black curve shows the sub-solar latitude while the more varied orange curve shows the sub-Earth latitude. The horizontal dashed curves are drawn at $\pm 8\overset{\circ}{.}4$. If the absolute value of the latitude is less than this angle, mutual eclipses can be seen. Superimposed on the plot are a series of vertical lines representing epochs of different data sets. The purple lines in 1996 and 2011 show when the light curves from Mueller et al. (2010) and Oey (2012) were taken. Note that the geometry was very similar for these two data sets. The green lines in late 2001, early 2002, 2005 and 2013 mark times of resolved ground-based AO observations. The thick red line in 2006 is the time of the Mueller et al. (2010) infrared mutual event observations. Note that those data clearly showed a partial shadowing event with no occultation, consistent with the latitude values plotted. Also note that the Oey (2012) results specifically mention that mutual events are ruled out at the time of their observations. The importance of this point will become clear later in the paper.

Two of the principal formation mechanisms for binary asteroids in the outer solar system are capture and coeval formation (Noll et al. 2008; Nesvorný et al. 2010). It is now thought that we have examples of binaries formed by each of these mechanisms. Morbidelli et al. (2005) further suggest that Trojans may have been delivered to their current locations from the trans-neptunian region (TNO) during early giant-planet migration. The Patroclus binary could have formed in a similar fashion to existing TNO binaries, either elsewhere or in the current Trojan cloud. Large mass ratios seem to be more consistent with capture, while smaller mass ratios seem to be more consistent with formation as a binary. One key observational test used to distinguish these two cases rests on physical observations. Such parameters as density, composition, albedo, spectral characteristics, and surface regolith properties all can be used. In the Kuiper Belt, a preponderance of the binary objects are seen to have identical colors between their components, while the mean system colors exhibit the full range of colors seen in the entire population (Benecchi et al. 2009). In the case of Patroclus, the Mueller et al. (2010) results indicate very similar regolith properties. While this is very suggestive of similar properties and thus coeval formation, we have an incomplete understanding of regolith formation and evolution and this could mask underlying differences. Two other quantities that are important in distinguishing the two components are density and albedo. Of the two, albedo should be the most easily determined from occultation observations. Density is harder because another source of information is required to get the mass ratio of the components that can then be combined with the volume from occultation data. For this work, our focus is on improving our estimates of the sizes and shapes of the two components.

2. OCCULTATION PREDICTION

Most main-belt occultation predictions these days are based entirely on what is known as a "catalog prediction." In this type of prediction, the position of the star is taken from a suitable high-quality catalog and the position of the asteroid is computed from its known orbit. Together, these positions can be used to derive a prediction for the ground track of the shadow and used to deploy the observing teams. One can always make additional astrometric observations of both the star and asteroid to refine the ground track, but this is rarely done for main-belt asteroids due to the very large number of predicted events. It is common practice among the International Occultation Timing Association (IOTA) community to work entirely from catalog predictions and decide which events to try to observe based on broader scientific interest, often adjusting plans to deal with last minute weather conditions.

The prediction of a Jupiter Trojan occultation is slightly more difficult than a main-belt asteroid—they are roughly 2× further away and thus require 2× better precision on the star and asteroid positions. However, in the case of Patroclus, the prediction presents an additional challenge from the presence of its large satellite Menoetius. There have not yet been

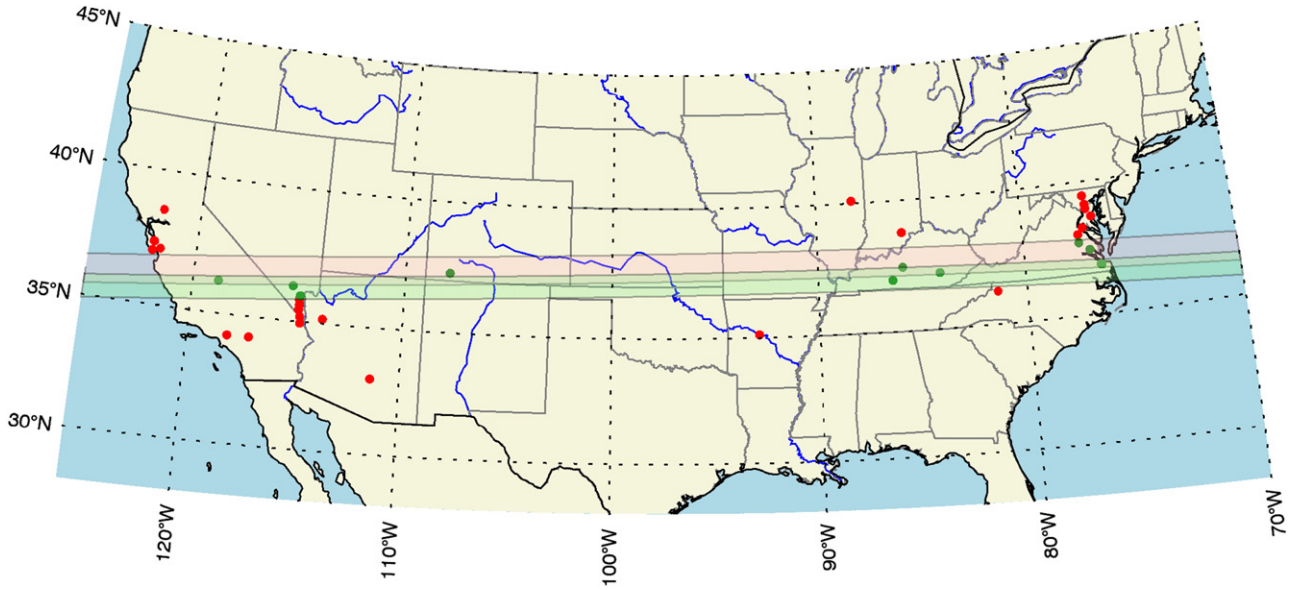

Figure 2. Ground track of Patroclus and Menoetius for 2013 October 21 occultation. The sites that collected useful data on the occultation or appulse are marked with dots. The red dots show stations that did not see any event. The green dots show stations that observed one or more discrete occultation events. The middle of the country was covered in cloud at the time of the event.

sufficient astrometry taken of Menoetius to fully constrain its orbit and position at a level needed for an occultation prediction. The fact that such observations require the very best AO-based facilities under good conditions makes the challenge even more severe. Thus, the prediction efforts for this event were entirely dominated by the quality of the mutual orbits of Patroclus and Menoetius around their center of mass. The actual ground track for the two components is shown in Figure 2.

In the weeks leading up to the event, a prediction was expected from F. Vachier (IMCCE/OBSPM), presumably based on the orbit of Marchis et al. (2006). But a few days before the event, the Vachier team was unable to provide a secure prediction that could safely target individual objects and a more conservative strategy was adopted. Operationally, the overall deployment strategy covered a range of positions as if we were trying to observe an object four times larger, and then adding on the basic uncertainty in the star and system barycenter. Upon learning of the prediction uncertainty, we turned to Keck AO imaging data, acquired in 2013 August by Merline's AO observing team (see acknowledgements), for just such a contingency. Those data, although of very high image quality, were not, in themselves, sufficient for a full orbit solution. But using some assumptions, an orbit was nonetheless derived and the positions of the components estimated. One outcome, apparent by simple inspection of the Aug 2013 AO data, was that the projected ellipse of the orbit on the sky was very elongated east–west, and this was true independent of orbital phase or of any orbit calculation. We therefore predicted a small N/S separation of the components (although the predicted phase of the components turned out, in hindsight, to be off by about 60° due to the rushed computations). Given the uncertainties in the orientation resulting from the rapid turn-around for this result, plus the basic track uncertainties, and given the difficulty of moving stations just before the event, it was recommended that observers not redeploy their stations. In the end, the stations were perhaps not optimally deployed north–south, but there were still a sufficient number within the actual track to map the size/shape of both components.

3. OBSERVATIONS

The occulted star was TYC 0646-00730-1 (UCAC2 36759189, GSC 00646-00730) with a brightness of $V = 9.61$ and $(B - V) = 1.60$. The time of geocentric close approach to the star was 2013 October 21 06:43:02 UT. At this time, Patroclus was 3.710 AU from the Earth and 4.674 AU from the Sun. The solar phase angle was 3°.39, solar elongation was 164°, and lunar elongation was 11°. The geocentric ephemeris position of Patroclus was R.A. of 02:47:58.8 and decl. of +14:06:00, J2000. For all observers, it was in the southern sky and well-placed within ±2 h of the meridian.

The large number of stations observing this event is a direct consequence of the efforts of IOTA. This organization is sanctioned by the International Astronomical Union and is comprised largely of amateur astronomers dedicated to the observation of stellar occultations by solar system objects. As a group, IOTA members world wide are quite active and successfully observe ~200 events per year. This particular event, due to the object being a Jupiter Trojan and a double object, commanded particular interest leading to a much larger deployment effort than is typical for the average asteroid event.

Within the IOTA observing community, the de facto deployment planning tool is OccultWatcher (OW; http://hristopavlov.net). This tool is freely distributed and is used to register for occultation events with each person's intended location (portable or fixed). As observers begin to sign up, OW provides a graphical view of the current prediction along with the chord placements along the ground track for known stations. In this way, interested observers can coordinate to fill the region needed and avoid either gaps in coverage or unnecessary duplication of effort.

The SwRI team chose to remain completely portable and uncommitted until no further delay could be tolerated. This allowed making a last minute decision based on best-case

coverage combined with the weather forecast across all of the planned sites. At the time there was a significant weather system moving across the southwest US. In the end, the final choice for the SwRI deployment was dictated more by the desire to reach an area that was likely to be clear somewhere within the greater shadow-path area.

Observations were attempted by a large group of IOTA participants and a few other interested teams. Most of the stations used video recording systems for their data. A complete summary of reporting stations and observations for this event is provided in Table 1. The first column is an event ID number. In some cases, two events were seen at one site, otherwise the ID number is also useful to identify the site. The observers and an indication of the observing site is shown in the second column. The next three columns give the WGS84 location of the telescope. Following the position is the start time and end time of the observation. If an event was observed, the time of ingress (disappearance) and time of egress (reappearance) are noted along with the timing uncertainty and the type of observation. Sites that made an attempt but were unable to collect data due to clouds or other issues are not included in this table. A few sites still use visual timings; these observations are reported but given little weight in the analysis. The timing for all the video data is provided by a video time insertion (VTI) device. This device takes an input video signal from the camera and then superimposes text on the video frame that contains accurate GPS-based time. This video overlay is also very useful in looking for dropped frames or other anomalies in the data. One such system is the IOTA-VTI that is the result of the efforts of IOTA members. This method is easily capable of providing timing that is good to at least a millisecond in absolute time, more than sufficient for the needs of this type of observation.

The cameras used are all low-cost high-sensitivity video cameras that range in price from $150 to $800. The higher-priced cameras generally support frame integration that give even better sensitivity at the expense of time resolution. All of these systems derive from high production-volume surveillance camera products, helping to keep the costs low. The target star in this case was relatively bright, bringing it in reach of very small optical systems. Many of the deployed sites were the so-called "Mighty Mini" systems designed by IOTA member Scott Degenhardt and deployed by Dunham and Maley for this event. These systems use a small lens on the camera and are mounted to a fixed tripod These systems are pre-pointed to the altitude and azimuth in the sky where the occultation will occur and then left to record on their own. The Mighty Mini is cheap and small enough that a sufficiently motivated observer can single-handedly deploy as many as ten stations. Other systems use more traditional tracking telescopes but these are almost always limited to one station per team.

The SwRI team used the equipment from the new Research and Education Collaborative Occultation Network (RECON) (Buie & Keller 2013; Keller & Buie 2013a, 2013b) designed for occultations by TNOs. This event was viewed as an excellent test case that mimics the type of occultation sought—a tight binary system with components that are roughly 100 km across. This system consists of a Celestron CPC1100 telescope (28 cm aperture), a MallinCAM B&W Special integrating video camera, an IOTA-VTI timing box, and a handheld mini-digital video recorder (mini-DVR).

Many other teams use camcorders for saving the video data but these devices are no longer made in a form that can be adapted to occultations. The data recorded by camcorders (even with analog tapes) are superior to the mini-DVR largely because the data-compression is too high on the mini-DVR. One result of this event was to clearly demonstrate the deficiencies of the mini-DVR, and RECON has now switched to using small portable computers with frame grabbers to collect data much like what is possible with camcorders. For all systems, the video data is eventually available as digital data that can be computer processed to retrieve light curves of the occultation event.

For all stations, the data consist of a few minutes of video. The start and end time of each recording is detailed in Table 1 along with notes about the observations where appropriate. There was a star nearby whose apparent brightness is similar to the occulted star that served as an on-chip reference star to remove any variable atmospheric extinction.

4. LIGHT CURVE ANALYSIS

Most of the occultation light curves were extracted using LiMovie or Tangra, free software products developed by Miyashita Kazuhisa and Hristo Pavlov. These tools perform sky-subtracted aperture photometry from the video images and return a digitized light curve, while reading the GPS timestamp on each frame to establish the absolute timing data. This process works perfectly for data taken with normal video frame rates. The process is slightly more complicated with frame-integrating video cameras. In this case, the video frame rate on the signal remains the same but the images copied to the video stream come from coadding frames internal to the camera prior to converting to a video signal. This method of increasing the integration time is always measured in frame (or field) times (e.g., 4-frame integration or 6-frame integration). This star was bright enough that there was little need for integration but some cameras still used it. The video time inserter unambiguously tags each video frame, but an additional step remains where the beginning of a integration period is identified.

There are two ways to discover the frame integration boundaries. The first is to have a sharply defined event in the scene (like an occultation). The transition where the star disappears will show a frame where the star is intermediate in brightness, caused by its disappearance during an integration. There will also be a grouping of nearly identical values for the derived star brightness that will match the frame integration length. On some cameras it is sufficient to note this grouping of identical measurements since the integrated video frame is precisely duplicated the requisite number of times (the Watec family of cameras falls in this category). Some cameras (like the MallinCAM) appear to be adjusting the signal or black level a small amount for every frame even through the replicated frames. In this case the replicated signal is very similar but not identical. Sometimes it is easy to tell where the integration boundaries are, sometimes not. Nonetheless, given a sharp event and a reasonable signal-to-noise ratio (S/N) it is always possible to unambiguously deduce the frame integration boundaries regardless of the vagaries of the cameras.

The second method for detecting frame integration boundaries is to use the background signal. The background is either sky signal or readout noise from the detector but the key element is the presence of pixel-to-pixel noise that is replicated within the integration period but changes between adjacent

Table 1
Observing Site and Occultation Timings

ID	Observers/Site	Longitude D:M:S	Latitude D:M:S	Alt (m)	Aper (cm)	Obs Start UTC	Obs End UTC	Ingress UTC	σ_I (s)	Egress UTC	σ_E (s)	Type
1	A Olsen, Urbana, IL	W088:11:46.5	N40:05:17.4	224	50	06:37:00	06:50:00	no event	⋯	no event	⋯	video
2	T Swift, Davis, CA, USA	W121:47:08.0	N38:33:08.2	18	20	06:41:40	06:53:00	no event	⋯	no event	⋯	video
3	S Conard, Gamber, MD	W076:57:06.1	N39:28:09.0	214	36	06:42:00	06:44:00	no event	⋯	no event	⋯	video
4	A Scheck, Scaggsville, MD	W076:53:13.5	N39:08:58.8	120	20	06:41:52	06:44:03	no event	⋯	no event	⋯	video
5	D/J Dunham, Greenbelt, MD	W076:52:09.5	N38:59:11.8	49	8	06:45:17	06:48:36	no event	⋯	no event	⋯	video
6	C Ellington, Owings, MD	W076:38:07.3	N38:41:26.0	47	25	06:40:00	06:47:00	no event	⋯	no event	⋯	video
7	R Venable, Crothersville, IN	W085:49:41.5	N38:46:40.6	172	35	06:42:55	06:44:53	no event	⋯	no event	⋯	video
8	Y Liu, Sunnyvale, CA	W122:03:33.2	N37:21:20.5	55	11	06:41:00	06:51:00	no event	⋯	no event	⋯	video
9	J Albers, Sunnyvale, CA	W122:02:20.0	N37:20:52.0	59	15	06:42:00	06:56:00	no event	⋯	no event	⋯	video
10	D Dunham/W Warren,Chestnut Hill, VA	W077:06:38.1	N38:17:21.8	50	8	06:41:07	06:45:56	no event	⋯	no event	⋯	video
11	D Breit, Morgan Hill, CA	W121:42:10.0	N37:06:47.8	282	30	06:38:42	06:56:00	no event	⋯	no event	⋯	video
12	D Dunham, Bowling Green, VA	W077:21:18.4	N38:03:02.9	59	8	06:40:20	06:46:30	no event	⋯	no event	⋯	video
13	R Nolthenius, Cave Gulch, CA	W122:04:45.2	N37:01:04.1	342	25	06:44:11	06:49:30	no event	⋯	no event	⋯	video
14	D Dunham, Hanover Courthouse, VA	W077:21:28.3	N37:44:40.9	42	8	06:39:48	06:46:05	06:43:18.44	0.02	06:43:20.20	0.02	video
15	M Croom/L Taylor, Barhamsville, VA	W076:52:08.6	N37:26:49.3	34	30	06:34:00	06:50:14	06:43:13.71	0.02	06:43:19.87	0.02	video
16	M Buie/C Olkin (SwRI), Durango, CO	W107:52:49.7	N37:17:06.3	2003	28	06:43:30	06:47:30	06:45:54.24	0.01	06:46:01.61	0.01	video
17	R Venable, Upton, KY	W085:52:52.9	N37:27:14.2	236	20	06:42:41	06:45:14	06:44:00.03	0.01	06:44:07.33	0.01	video
18	R Royer, Springville, CA	W118:48:45.5	N36:12:40.3	533	32	06:44:00	06:49:00	06:46:49.70	0.3	06:46:55.20	0.3	VISUAL
19	R Royer, Springville, CA	W118:48:45.5	N36:12:40.3	533	32	06:44:00	06:49:00	06:46:10.00	0.3	06:46:16.20	0.3	VISUAL
20	H Abramson/K Abramson, Chesapeake VA	W076:25:40.0	N36:51:20.1	8	24	06:35:30	06:45:36	06:43:11.02	⋯	06:43:16.12	⋯	video
21	H Abramson/K Abramson, Chesapeake VA	W076:25:40.0	N36:51:20.1	8	24	06:35:30	06:45:36	06:42:31.84	⋯	06:42:37.65	⋯	video
22	D Rowley, Chesapeake, VA	W076:23:33.3	N36:50:55.7	3	20	06:39:00	06:47:00	⋯	⋯	06:42:38.20	0.5	VISUAL
23	J Dunford, London, KY	W084:06:35.7	N37:08:56.4	394	20	06:39:11	06:49:47	06:43:52.05	0.02	06:43:55.71	0.02	video
24	J Dunford, London, KY	W084:06:35.7	N37:08:56.4	394	20	06:39:11	06:45:36	06:43:11.82	0.02	06:43:18.22	0.02	video
25	D Blanchette, Las Vegas, NV	W115:17:31.7	N36:19:27.3	805	30	06:40:00	06:50:00	06:45:52.37	0.17	06:45:59.20	0.17	video
26	R Venable, Bowling Green, KY	W086:23:32.9	N36:58:40.3	160	13	06:42:36	06:45:40	06:43:23.37	0.01	06:43:30.05	0.01	video
27	Predicted Centerline w/Time	W078:00:00.0	N36:34:55.0	0	⋯	⋯	⋯	06:42:57.70	⋯	06:43:06.30	⋯	video
28	E Bredner/B Wickord, Las Vegas NV	W114:54:35.5	N35:58:17.1	707	10	06:30:00	06:50:00	06:45:52.08	0.04	06:45:57.68	0.04	video
29	P Maley, Las Vegas NV	W114:55:13.5	N35:54:36.1	1720	8	06:42:00	06:50:00	no event	⋯	no event	⋯	video
30	R Lambert, Boulder City, NV	W114:56:10.5	N35:49:39.6	500	13	06:42:00	06:52:00	no event	⋯	no event	⋯	video
31	D Caton, Boone,NC	W081:24:44.0	N36:15:05.0	1000	81	06:42:18	06:44:18	no event	⋯	no event	⋯	drift
32	P Maley/J Stein, Las Vegas NV	W114:54:42.1	N35:38:05.2	850	8	06:42:00	06:50:00	no event	⋯	no event	⋯	video
33	P Maley/J Shull, Las Vegas NV	W114:56:11.7	N35:26:59.7	1120	8	06:42:00	06;50:00	no event	⋯	no event	⋯	video
34	P Maley/J Crumpley, Las Vegas NV	W114:51:06.3	N35:11:18.9	30	5	06:42:00	06:50:00	no event	⋯	no event	⋯	video
35	L Fleming,Kingman AZ USA	W113:46:48.0	N35:10:12.0	1280	2	06:40:00	06:52:00	no event	⋯	no event	⋯	video
36	P Maley/J Pierce, Las Vegas NV	W114:49:25.2	N34:56:34.5	1720	8	06:42:00	06:50;00	no event	⋯	no event	⋯	video
38	B Owen/S Preston, Altadena, CA	W118:08:05.6	N34:12:19.5	387	12	06:45:20	06:48:00	no event	⋯	no event	⋯	video
39	R Jones,Running Springs, CA	W117:07:52.4	N34:13:07.9	1844	20	06:41:00	06:51:00	no event	⋯	no event	⋯	video
40	C Sherrod,Morrilton, AR	W092:55:00.5	N35:07:10.8	89	51	06:43:45	06:46:00	no event	⋯	no event	⋯	video
41	W Thomas, Florence, AZ	W111:21:00.6	N33:00:54.4	184	27	06:45:02	06:47:00	no event	⋯	no event	⋯	video

Note. Latitude and Longitude are on the WGS84 datum.

integrations. The only requirement on the system is that the background level be preserved as well as the noise in the background. Under these circumstances the integrations can be uniquely identified as well as dropped frames in the recorded video signal, even without a sharp event in the data. The video camera systems always seem to preserve the data quality and have no dropped frames, hence the preference for this tool among the IOTA community. Computer-based frame grabbers can do similarly well if the proper settings are used. However, there are many settings, most involving high degrees of lossy compression, that will make the data very difficult to process. The mini-DVR is the worst of the bunch. This device is very small, low-cost, and low-power, and very simple to operate making it an attractive option. These features come at a price. First, the range of the video signal is shifted as if the brightness were being turned down. The consequence to the data is that the sky background in most cases is reduced to a level below zero and comes out as a uniform hard black level of zero. Second, the mini-DVR records at a low data rate using a lossy compression protocol designed to minimize the file size stored to the memory card. The RECON mini-DVR does have some controls (high, medium, and low) on the compression but even at its lowest compression setting the data quality is noticeably affected. Finally, the mini-DVR records only one field within the interlaced frame. The consequence of this is that the odd rows in the image are a copy of the even rows (or vice versa) thus throwing away half of the photons that are collected. We presume this is due to the need to find time for the mini-DVR to do the compression since it is obviously not a high-powered computing device. For this event, these problems could be overcome due to the brightness of the target star but in general the mini-DVR option is of limited value for recording occultation data, especially for faint events. In this case, the Patroclus event was very bright and adequate data were obtained.

Once all light curves are digitized, the time of disappearance (D) and reappearance (R) are extracted from the data. If the star is sufficiently small the transition from visible to not visible will be essentially instantaneous. Technically, a Fresnel diffraction pattern should be visible but these video camera systems rarely have the photometric precision to see this effect, regardless of the brightness of the occulted source. If the star turns out to be double or if it has an apparent size large enough then we see a more complicated pattern in the data. In the case of this star, it became readily apparent the transition was slower, indicating that the angular size of the star was being detected. To get the timing from the data requires fitting for the size of the star along with the precise times from each chord. Of course, the size is a constant across all stations and can be imposed on poorer quality data based on the results from higher S/N light curves. From the fitting, the size of the star was determined to be 0.69 ± 0.03 mas. For reference, the angular scale at the distance of the asteroid was 2691 km arcsec^{-1} making the projected size of the star 1.9 km at the time of the event. The sky-plane velocity of the asteroid was 6.1 mas s^{-1} or 16.4 km s^{-1}. The D and R times are tabulated in Table 1. It was immediately obvious from this part of the analysis that chords were obtained on two similarly sized objects. Some stations were able to get chords on both objects.

Some representative examples of the light curve data collected are shown in Figure 3. The traces are ordered from north to south with the observer and event ID(s) noted to the right. Some of the negative observations (those in which data were collected but an occultation event was not seen) are also shown to provide an indication of the data quality. This relatively bright star was an easy target for the usual IOTA system. Standard practice among the IOTA community is for each observing team to process their own data and then file an observing report form for their station. This electronic form encourages and reminds the observers to provide information on the observing team, observing location, and equipment used, as well as the final occultation event timing. This standard process does not provide a standardized way to post the original video data or require the submisison of extracted light curves. Even so, this process proves good enough on most routine main-belt asteroid events.

The Patroclus–Menoetius event was unusual in two respects. Double asteroids with a high likelihood of observing both components, along with its intrinsic interest to the scientific community, contributed to a very large number of participating stations. Also contributing to the interest was the brightness of the star, permitting useful observations wit small aperture systems. The brightness of the star has a downside. As is typical with bright star events, the apparent angular size of the star is large enough to affect the shape of the occultation event. Those processing the data for this event realized quickly that the star was indeed slightly resolved by our occultation data thus requiring a more careful analysis than simply reading off the time of disappearance and reappearance from the time tagged video data.

5. LIMB-FITTING

Given the D and R times plus the locations of all the observing stations, it is a simple matter to co-register these chords onto the plane of the sky at the asteroid. Each chord provides two constraints on the limb of the object. With sufficient density of chords, as in this case, we can then find a best fitting ellipse. Given that we have data on two objects, the chords also provide accurate relative separations between the objects at the time of the event.

The orbital motion of the two components is slow compared to the occultation event. Mueller et al. (2010) indicate an orbital period of about 103 h and semimajor axis of about 654 km. The orbital speed is thus 11 m s^{-1}. The earliest ingress time was 06:42:31.84 UT and the latest egress time was 06:46:55.20 UT. Since the chords are not obtained all at the same time, there is 2.9 km of motion along the orbit as the shadow crossed the network of stations. This amount of motion is neglected, even though it could be important at the right orbital longitude. In our case, the motion is more nearly along the line of sight and is of less concern.

Figure 4 shows the combined limb fits on the fundamental plane. These fits were derived using Occult4 (http://www.lunar-occultations.com/iota/occult4.htm). The origin of this coordinate system is set by the final prediction using the known star position and the asteroid orbit assuming it is one body. There is no physical benefit in this choice of origin, but was merely computationally convenient. In this frame fixed on the Patroclus system, the star appears to move from right to left. The western component is Menoetius and the eastern is Patroclus.

The identity of the components is ultimately based on the AO imaging data. In all cases, one of the components appears to be consistently brighter. This one is considered to be

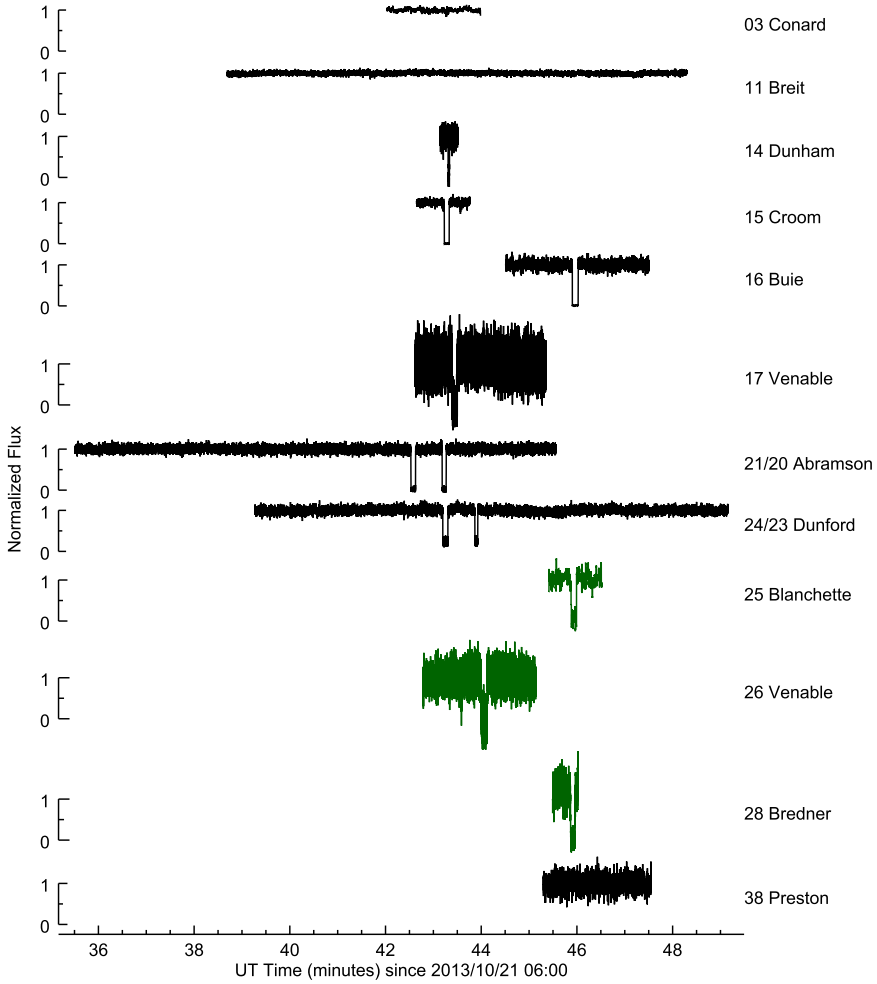

Figure 3. Occultation light curves. These plots depict the light curves from which the occultation timings were derived. Some negative events are shown for reference. The sites where events from both components were seen are immediately obvious with the first object seen being Menoetius. The single object events involving Menoetius are plotted in green. No temporal filtering has been applied to these light curves. However, some data sets were collected with integrating cameras and these will appear to have lower noise. All curves are calibrated for the stellar flux between zero (occulted) and one (unocculted).

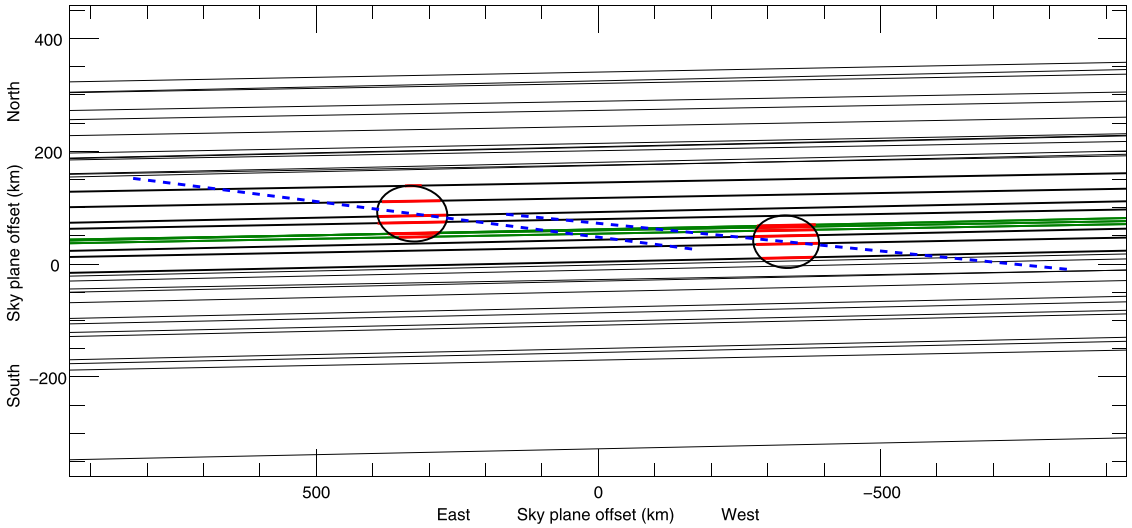

Figure 4. Ellipsoidal limb fits and relative spacing for Patroclus and Menoetius for 2013 October 21 occultation. The thick red segments indicate when the star was occulted. The thinner lines across the plot indicate the region probed by each station. The green lines indicate the tracks that intersected both objects from a single site. The blue dashed lines show the fitted angle for the long axis of each object. This result is consistent with alignment of the major axes of both objects that would be expected for a fully tidally evolved system.

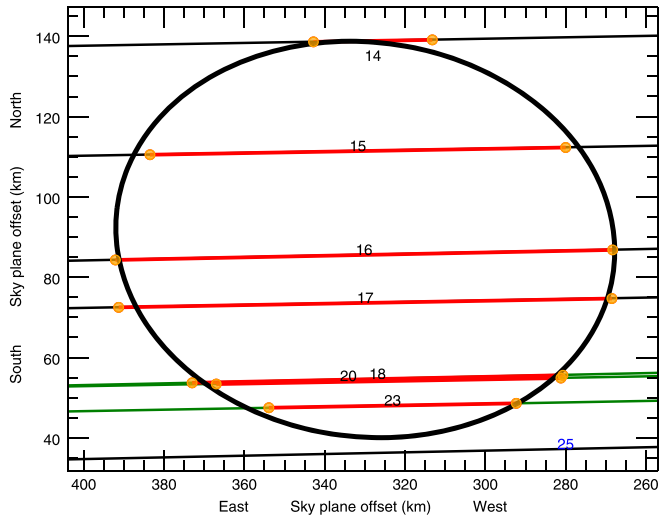

Figure 5. Ellipsoidal limb fit to Patroclus chords for 2013 October 21 occultation. The numbers indicate the event ID from Table 1. The orange (filled) dots indicate the measured disappearance and reappearance events. The thick red segments indicate when the star was occulted. The thinner lines across the plot indicate the region probed by each station. The green lines (18, 20, and 23) indicate the tracks that intersected both objects from a single site. The timing errors are at or below the size of the symbols at the ends of the chords for all video data.

Patroclus, the primary. We thus identify the larger object as Patroclus. This assignment will be valid provided that there are no large differences in albedo between the two objects. With sufficiently resolved astrometric data, the identity can be unequivocally determined but this is beyond the scope of the present work. For the remainder of this work, we assume these identities are secure.

The limb fits give a J2000 differential sky-plane position for Patroclus of (329.9, 89.4) km with a projected ellipse of 124.6 by 98.2 km, projected axis ratio of 1.27, and a position angle of the major axis of the ellipse of 82°.8, measured eastward from north. The values for Menoetius are a position of (−332.8, 39.6) km with a 117.2 by 93.0 km ellipse, projected axis ratio of 1.26, and a position angle of 84°.4. Within the uncertainties of the limb fit, this result is consistent with a tidally evolved pair where both object's long axes are co-aligned. Menoetius is 664.6 km (0.247 arcsec) from Patroclus at a position angle of 265°.7 measured eastward from north in a J2000 coordinate system.

The results for Patroclus plotted in Figure 5 show a projected limb profile. Of the plotted chords, only #18 is a visual chord. All of the others are based on GPS-based video timing. The formal uncertainties in the video timing are all below 1 km. The visual chord is estimated to have a 1-σ uncertainty of about 3 km. The agreement between #18 (visual) and #20 (video) is quite good and consistent with these errors. The video chords clearly do not exactly match the ellipse fit with the largest discrepancy being at the northern limb with chord #14. These observations indicate deviations in shape from an ellipsoid (possibly just local topography) on a scale of 5 km.

The results plotted for Menoetius in Figure 6 are very similar to the Patroclus results except for a pair of non-detections (stations 29, 30). Again, the fitted ellipse is shown for this body but the ellipse is constrained only by the chords that were observed. Here we also have one visual chord, #19 that is the most discrepant of all the chords being off the limb fit by ∼10 km. Given its proximity to #21 the deviation of the visual chord from the limb is most likely due to an error in recording the start time of the event. Note that the visual chords (#18 & #19) were made by the same observer and the discrepant time is the first of the four event timings to be recorded. Of the video chords, the most deviant is #26 which again suggests variations on the order of 5 km from an ellipsoidal shape.

The lack of a Menoetius event for track #17 (which did see Patroclus) is easily explained as a near miss on the northern limb. This non-detection was not used as a constraint on the limb fit but the derived geometry is consistent with a miss, further confirming the elliptical profile. Had this site been positioned just 5 km south it would have most likely resulted in a double chord. The lack of events for tracks #29 and #30 are not so easily explained. Assuming an ellipsoidal shape and the location of those tracks, an event should have been visible from both sites. The observers both submitted reports of a miss and were confident in the star field observed. All data were recorded on video tapes and reviewed but due to the lack of event no light curves were ever extracted. Unfortunately, the tapes were never formally digitized and were subsequently recorded over before work began on this paper when the relevance of the non-detections were realized. It was certainly noted at the time that there was a rather long chord from site #28 and that the two "missing" chords really should have been positive. This situation underscores the importance of retaining all video data from occultations with negative chords as well as positive chords.

Taken at face value, the non-detections for the stations #29 and #30 indicate a large void in the shape of Menoetius. To explore this conclusion further, Figure 6 includes some extra markings. The faint dashed lines indicate the major axis (mostly east–west) and the minor axis (mostly north–south) which are derived from the ellipsoidal limb fit. Imagining the void to be bound by a straight line, there are two extra lines drawn in between the chord from site 28 and the reported null observation from site 29. These two lines show the extremes of such a straight line limb projection that are consistent with the detection of #28 and the non-detection of #29. The inferred shape implied by the hypothetical void is entirely consistent with a large impact basin on Menoetius, very similar in relative size to the feature seen on the south pole of Vesta (Jaumann et al. 2012). In a tidally evolved system, it makes the most sense for this void to be centered on the minor axis. This placement is also required to "hide" it from light curve photometry. The dot–dash teal line is obviously not orthogonal to the rotation axis and can be ruled out on the basis of the extremely symmetric light curve. The solid teal line is parallel to the major axis to within one degree. If the reported misses are valid, the lack of occultations at these two sites imply a void (perhaps a crater) on the southern limb that is at least 18 km in depth. The true depth cannot be measured with these occultation data and really is a lower limit to the depth from the projected limb to the bottom of the excavation. This interpretation of the non-detections requires, however, that the sub-Earth latitude of the system at the time of the occultation be within a degree or so of the object's equatorial plane in order to not be apparent in the rotational light curve data. This geometry would imply that the system is always experiencing mutual events. Mutual events were seen in 2006 and 2012 and the light curve photometry rules out mutual events in 2011. When combined, these constraints preclude such a low sub-Earth

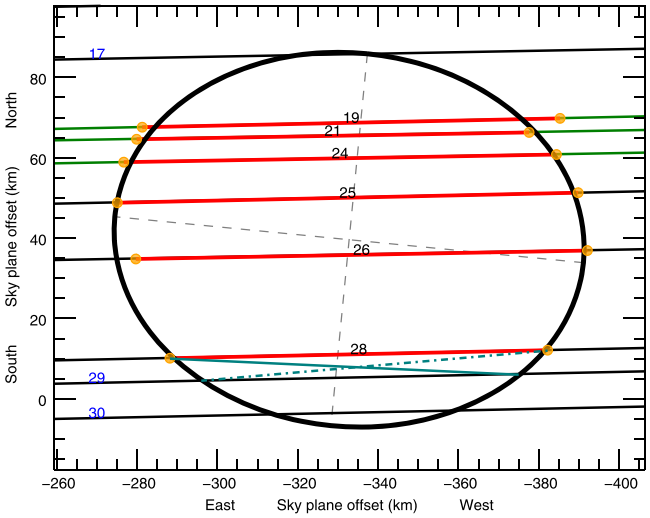

Figure 6. Ellipsoidal limb fit to Menoetius chords for 2013 October 21 occultation. The numbers indicate the event ID from Table 1. The orange (filled) dots indicate the measured disappearance and reappearance events. The thick red segments indicate when the star was occulted. The thinner lines across the plot indicate the region probed by each station. The green lines (19, 21, and 24) indicate the tracks that intersected both objects from a single site. The timing errors are at or below the size of the symbols at the ends of the chords for all video data. See the text for additional discussion.

latitude at the time of the occultation. We are forced to conclude that the non-detections were false but in the absence of the original data can provide no satisfactory explanation for the apparent miss. Whatever the real explanation is for these two non-chords, additional photometric data (rotational light curves and mutual event light curves) can easily place strong constraints on the shape and eventually resolve this mystery.

6. DISCUSSION

We return now to the viewing geometry implied by Figure 1. On 1996 April 16 the sub-Earth latitude was 15°.6 and the sub-solar latitude was 16°.7. This is the geometry for the photometry shown in Mueller et al. (2010) where they observed a 0.070 ± 0.005 mag amplitude light curve. From this, they infer 1.07 :1.0 :1.0 for their ellipsoidal shape. A second epoch of photometry by Oey (2012) covers the time range of 2011 August–September, where the light curve amplitude was determined to be 0.06 ± 0.02 mag. At the reference time for that work (JDo = 2455783.9), the sub-Earth latitude was 25°.8 and the sub-solar latitude was 20°.0. The geometries for these two epochs of data are similar and the light curve amplitudes are consistent within the errors. The Oey (2012) data have a lower amplitude which is consistent with the slightly higher latitude but the uncertainties are too large to provide a strong constraint in any change in the light curve. At the time of the occultation, the sub-Earth latitude was −20°.6 and the sub-solar latitude was −21°.0. Assuming a symmetric object, the projected limb at the time of the occultation was very similar to that for all of the photometry. Note that the pole solution we are using still suffers from the orbit mirror ambiguity, but the only real consequence is to swap north with south. We believe a better orbit that also eliminates the mirror ambiguity can be generated but this refinement is not required to understand the occultation data and is beyond the scope of work presented here.

To investigate the three-dimensional shape of these bodies, we computed a simple shape model. In this model we assumed that the shape for each object is similar, differing only in scale. The model includes plausible Hapke scattering parameters with an albedo similar to that derived by Mueller et al. (2010). This model incorporates a reasonable approximation to its photometric behavior at the observed solar phase angle. This model is not intended to be a precise tool but rather to demonstrate rough trends and sensitivities to shape. With this model, a shape of 1.07 :1 :1 at 15°.6 latitude exhibits a symmetric light curve with an 0.074 mag amplitude consistent with the assertions of Mueller et al. (2010). At 10° the amplitude increases to 0.078 mag and At 20° the amplitude drops to 0.072 mag. At 30°, the amplitude drops to 0.060. Outside of the range where mutual events occur, the dependency of the light curve amplitude on geometry is very small. This shape is clearly consistent with the two light curves.

The occultation indicates a projected ellipse of 1.26:1 which, if the shape were prolate as suggested by Mueller et al. (2010), would imply axial ratios of 1.26 : 1 : 1 regardless of the sub-Earth latitude at the time of the occultation. This shape is significantly more elongated than the prolate shape from Mueller et al. (2010) and implies a light curve amplitude that is 26%, a value inconsistent with the light curves. We thus require a larger intermediate axis to reconcile the occultation and light curve data. If the object were purely oblate there would be no rotational light curve thus implying the three principal axes must be different. The occultation occurred very near maximum elongation and thus directly constrains the major axis of the ellipsoid. The light curves set the ratio of the intermediate axis to the major axis of the ellipsoid. Taking the sub-Earth latitude at the time of the occultation to be −21°, the ratio of the polar (minor) axis to the major axis must be 1.3 after deprojection. The combined constraint thus sets the axial ratios to be 1.3 : 1.21 : 1. This shape would be aligned such that the longest axis is aligned with the Patroclus–Menoetius line and the shortest axis is aligned with the angular momentum vector. The maximum light curve amplitude for this shape is about 8% and the minimum amplitude would be about 4%. This shape also predicts very similar light curve amplitudes for the two epochs constrained by photometry.

A shape model consistent with the occultation and light curve data is shown in Figure 7. This rendering uses plausible Hapke parameters to get a reasonable illumination and limb-darkening but these are not best-fit parameters. This particular model reproduces a 6% light curve amplitude with symmetric minima and maxima at ±20° latitude. The bodies are shown with an equator-on view where the elliptical projection of the body is the most pronounced. When viewed from the same latitude as seen at the time of the occultation, the projected ellipse is slightly less elongated and matches the observed limb-fit. This figure shows both objects to the same scale. The single-scattering albedo for each tile in the shape model has a small random component for illustrative purposes.

This shape model has mean-ellipsoidal axes of $127 \times 117 \times 98$ km for Patroclus and $117 \times 108 \times 90$ km for Menoetius. The total volume of both bodies is 1.36^6 km^3. Combining this volume with the mass of 1.20×10^{18} kg (Mueller et al. 2010) provides a system density of 0.88 g cm^{-3}. A volume-equivalent spherical size for Patroclus is $D_1 = 113$ km and Menoetius is $D_2 = 104$ km. Combining these sizes into a effective mean projected area gives

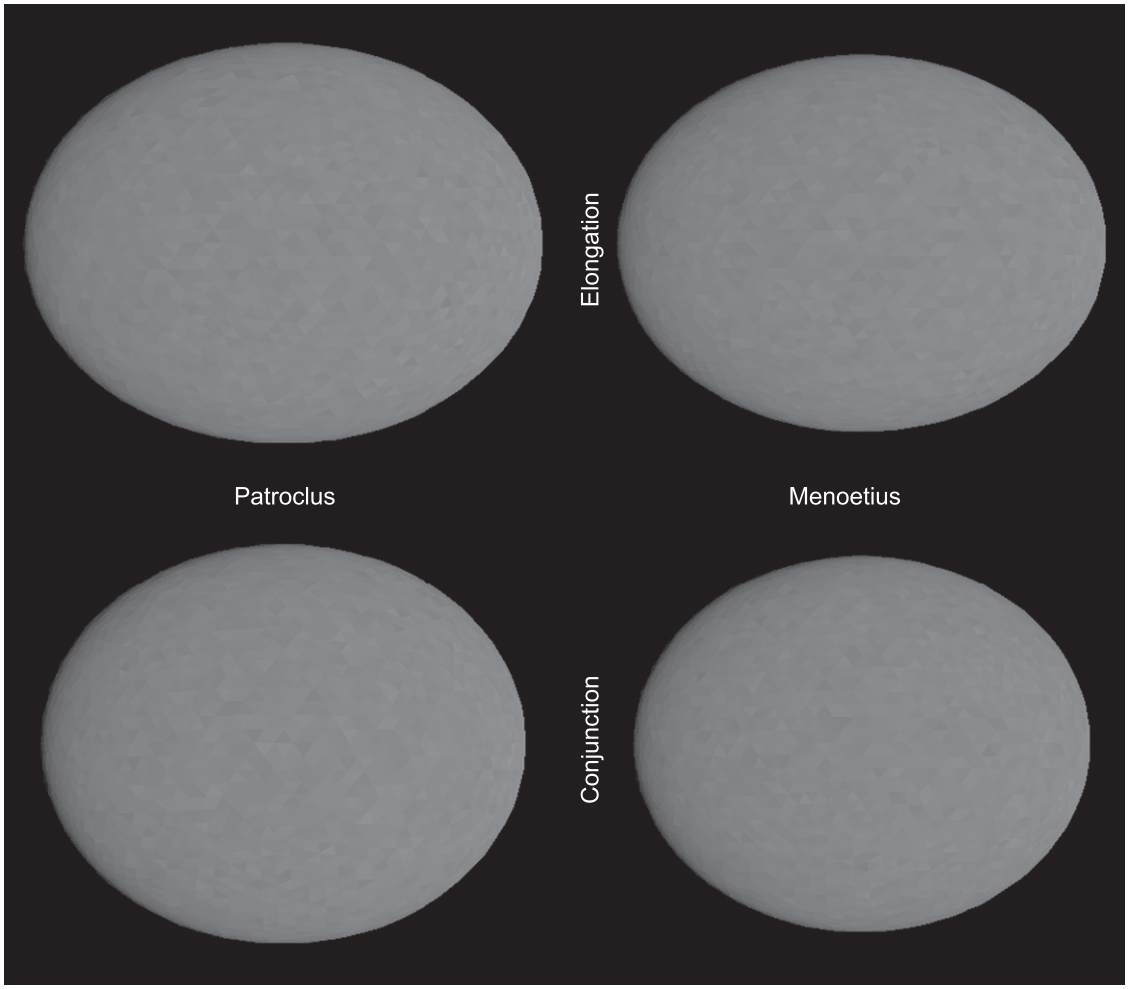

Figure 7. Shape of Patroclus and Menoetius inferred from occultation and light curve constraints. The two images on the left are for Patroclus and the images on the right are for Menoetius. The top images are at maximum elongation which is coincident with the maximum projected area. The bottom images show the projected area at conjunction, 90° of orbital longitude later. The relative sizes of the two objects is preserved. The sub-Earth latitude of this rendering is 0° and a solar phase angle of 5°.

$D_A = 154$ km. These numbers can be compared with those from Mueller et al. (2010) of $D_A = 145 \pm 15$ km, $D_1 = 106 \pm 11$ km, $D_2 = 98 \pm 10$ km and both sets are consistent as well as the ratio of the equivalent diameters.

In light of this result regarding the shape of Menoetius it may well be worth a reconsideration of the *Spitzer* results from Mueller et al. (2010). Those data depend on understanding the projected area during their observations. Also, getting precise photometry of both components would now allow a better estimate of the albedo of each body. Combining the constraints provided by thermal radiometry, photometry, and occultations will allow a more precise test to see if the albedos and thermal properties of the regolith are truly the same between the two bodies.

The component shapes and spins and their mutual orbit can help to probe the system's formation and evolution. The total angular momentum of the system is very high, such that if all of the mass and angular momentum were sequestered into a single sphere it would be spinning well beyond the breakup spin limit (see Pravec & Harris 2007; it has nearly twice the angular momentum that the sphere could absorb). Therefore the system's origin is not from a single disrupted body, unless there were significant increases of angular momentum to the system over time. The known processes of YORP and BYORP can increase the angular momentum of single bodies or systems (Bottke et al. 2006) but are unlikely to affect large and distant systems.

The oblate shapes of the two components of the binary relative to fluid equilibrium perhaps provides stronger constraints on their origin. Similar to the non-hydrostatic shape of the Saturnian moon Iapetus (Castillo-Rogez et al. 2007), these bodies might have suffered a substantial amount of heating and melting in their history, and their shapes are suggestive of a faster rotation rate at the time they cooled. If this binary system were formed with an initially closer separation and tidally evolved outward to the current doubly synchronous state, the axis ratios and oblate shapes suggest rotation rates on the order of 6–9 h (Castillo-Rogez et al. 2007), which would correspond to binary separations of 7–8 $a(R_{\rm pri})$ with the current system angular momentum for $P = 103$ h at $\sim 12\, a(R_{\rm pri})$.

Meanwhile, if the system shares an origin with the KBO binary systems, then the Nesvorný et al. (2010) mechanism of binary formation via direct collapse of material could be the origin of the high system angular momentum content as well as the shapes of the components. Many of the observed binary

systems in the Kuiper Belt have even more angular momentum than the Patroclus system (see Table 2 of Noll et al. 2008 for examples). In addition, Richardson et al. (2005) find that collapsing clouds of granular material (making up rubble pile asteroids) typically collapse to fluid equilibrium shapes, even when the assembled body can maintain more extreme shapes owing to the angle of friction on its surface. Thus, again, the Nesvorný et al. (2010) mechanism could have produced a system with an initial binary separations of 7–8 $a\,(R_{\rm pri})$ and the correct shapes, that tidally evolved to the system we see today.

There are few Hot Classical systems of this size in the Kuiper Belt. If Patroclus was formed in the primordial Kuiper Belt and subsequently scattered into the Trojan population (Morbidelli et al. 2005; Nesvorný et al. 2013), it is fair to ask why it survived the trip. According to the binary formation simulations of Nesvorný et al. (2010), this system's separation of less than 1000 km is among the tightest that would be formed from this mechanism, and this may correlate directly with survival likelihood. The oblate shapes seemingly argue against the collapse of a looser binary that tightened during tidal evolution, as very slowly rotating components would be expected to have much more spherical shapes.

7. CONCLUSIONS

Clearly additional occultation data would be useful to confirm these results but it is possible to do this in other ways. Every 6 yr there is a season of mutual events between Patroclus and Menoetius. The first observed season was in 2006 and the only published result from this is Mueller et al. (2010). In that reference there is mention of a meeting abstract (Berthier et al. 2007) but those observations are as yet unpublished and do not appear to be available to the community. The next season will be in 2018, though a detailed prediction should be done on updated orbital elements. A well-observed mutual event season as well as more complete rotational light curve coverage will allow an excellent opportunity to improve our understanding of this intriguing object.

Thanks go to many IOTA members contributing to this effort for observing: J. Albers, D. Blanchette, E. Bredner, J. Crumpley, J. Dunham, L. Fleming, R. Jones, R. Lambert, C. McPartlin, R. Nolthenius, J. Pierce, D. Rowley, J. Shull, J. Stein, W. Thomas, W. Warren, and B. Wickord. Special thanks to Hristo Pavlov for his work developing and supporting OccultWatcher that plays a crucial role in efficiently coordinating occultation campaigns worldwide. The 2013 Keck AO data and analysis were provided by Merline's AO observing team: Observations—Bill Merline, Peter Tamblyn, Al Conrad, Julie Tamblyn; Orbit computation—Bill Owen; Support—Benoit Carry, Jack Drummond, Clark Chapman, Brian Enke, Julian Christou. The shape model tools used in this work were developed in IDL by Will Grundy. We also acknowledge the open source software community for tools used in this work: Vim/gVim, openOffice, and Fvwm2 as well as the tools associated with Google Drive.

REFERENCES

Benecchi, S. D., Noll, K. S., Grundy, W. M., et al. 2009, Icar, 200, 292
Berthier, J., Marchis, F., Descamps, P., et al. 2007, BAAS, 39, 482
Bottke, W. F., Jr., Vokrouhlický, D., Rubincam, D. P., & Nesvorný, D. 2006, AREPS, 34, 157
Buie, M. W., & Keller, J. M. 2013, AAS/Division for Planetary Sciences Meeting Abstracts, 45, #511.08
Castillo-Rogez, J. C., Matson, D. L., Sotin, C., et al. 2007, Icar, 190, 179
Jaumann, R., Williams, D. A., Buczkowski, D. L., et al. 2012, Sci, 336, 687
Keller, J., & Buie, M. W. 2013a, AAS/Division for Planetary Sciences Meeting Abstracts, 45, #414.12
Keller, J. M., & Buie, M. W. 2013b, AGU Fall Meeting Abstracts, ED51D-09
Marchis, F., et al. 2006, Natur, 439, 565
Merline, W. J., Close, L. M., Siegler, N., et al. 2001a, IAUC, 7741, 2
Merline, W. J., Close, L. M., Menard, F., et al. 2001b, BAAS, 33, 1133
Merline, W. J., Weidenschilling, S. J., Durda, D. D., et al. 2002, in Asteroids III, ed. W. F. Bottke, Jr. et al. (Tucson, AZ: Univ. Arizona Press), 289
Morbidelli, A., Levison, H. F., Tsiganis, K., & Gomes, R. 2005, Natur, 435, 462
Mueller, M., Marchis, F., Emery, J. P., et al. 2010, Icar, 205, 505
Nesvorný, D., Vokrouhlický, D., & Morbidelli, A. 2013, ApJ, 786, 45
Nesvorný, D., Youdin, A. N., & Richardson, D. C. 2010, AJ, 140, 785
Noll, K. S., Grundy, W. M., Chiang, E. I., Margot, J.-L., & Kern, S. D. 2008, in The Solar System Beyond Neptune, ed. M. A. Barucci et al. (Tucson, AZ: Univ. Arizona Press), 345
Oey, J. 2012, MPBu, 39, 107
Pravec, P., & Harris, A. W. 2007, Icar, 190, 250
Richardson, D. C., Elankumaran, P., & Sanderson, R. E. 2005, Icar, 173, 349